ELSEVIER

Available online at www.sciencedirect.com

SCIENCE DIRECT

Advances in Water Resources 29 (2006) 1351–1370

Advances in Water Resources

www.elsevier.com/locate/advwatres

Upscaling geochemical reaction rates using pore-scale network modeling

Li Li, Catherine A. Peters *, Michael A. Celia

Department of Civil and Environmental Engineering, Princeton University, Princeton, NJ 08544, USA

Received 19 May 2005; received in revised form 14 October 2005; accepted 20 October 2005
Available online 6 December 2005

Abstract

Geochemical reaction rate laws are often measured using crushed minerals in well-mixed laboratory systems that are designed to eliminate mass transport limitations. Such rate laws are often used directly in reactive transport models to predict the reaction and transport of chemical species in consolidated porous media found in subsurface environments. Due to the inherent heterogeneities of porous media, such use of lab-measured rate laws may introduce errors, leading to a need to develop methods for upscaling reaction rates. In this work, we present a methodology for using pore-scale network modeling to investigate scaling effects in geochemical reaction rates. The reactive transport processes are simulated at the pore scale, accounting for heterogeneities of both physical and mineral properties. Mass balance principles are then used to calculate reaction rates at the continuum scale. To examine the scaling behavior of reaction kinetics, these continuum-scale rates from the network model are compared to the rates calculated by directly using laboratory-measured reaction rate laws and ignoring pore-scale heterogeneities. In this work, this methodology is demonstrated by upscaling anorthite and kaolinite reaction rates under simulation conditions relevant to geological CO_2 sequestration. Simulation results show that under conditions with CO_2 present at high concentrations, pore-scale concentrations of reactive species and reaction rates vary spatially by orders of magnitude, and the scaling effect is significant. With a much smaller CO_2 concentration, the scaling effect is relatively small. These results indicate that the increased acidity associated with geological sequestration can generate conditions for which proper scaling tools are yet to be developed. This work demonstrates the use of pore-scale network modeling as a valuable research tool for examining upscaling of geochemical kinetics. The pore-scale model allows the effects of pore-scale heterogeneities to be integrated into system behavior at multiple scales, thereby identifying important factors that contribute to the scaling effect.

Keywords: Pore-scale network modeling; Reactive transport modeling; Upscaling; Geochemical kinetics; Geological CO_2 sequestration

---

1. Introduction

Geochemical modeling of reactive transport of chemical species in subsurface systems has been widely applied to improve our understanding of the complex processes involved in fluid–rock interactions [1–3], and to solve environmental problems related to groundwater and subsurface contamination [4–7]. Reactive transport modeling is generally classified into forward modeling and inverse modeling [8]. Forward modeling predicts the transport and reaction of chemical species given specified geochemical reactions and reaction rate parameters. Inverse modeling utilizes measured chemical compositions to infer geochemical reactions that have occurred along flow paths. These two types of modeling approaches serve as powerful tools to understand, predict, and interpret reactive transport of chemical species in subsurface environments, and provide insights into possible regulation and management strategies.

---

* Corresponding author. Tel.: +1 609 2585645; fax: +1 609 2582799.
E-mail address: cap@princeton.edu (C.A. Peters).

doi:10.1016/j.advwatres.2005.10.011

EXHIBIT
tabbles
60

Because reactive transport modeling is typically applied at large scales, it necessarily ignores spatial heterogeneities at scales smaller than the size of model discretization. For mineral dissolution and precipitation, there is a mismatch between the scale at which rate data are needed (the scale of model discretization) and the scale for which rate data are available. Mineral dissolution and precipitation is typically modeled using geochemical reaction kinetics measured in laboratory systems that are very different from natural systems. In the laboratory, geochemical reaction rates are typically measured in well-mixed systems using crushed mineral suspensions [9]. These experiments are intentionally designed to homogenize mineral samples and to eliminate aqueous-phase mass transport limitations. This way the aqueous concentrations reflect reaction progress and can be used to determine the forms and parameters of reaction rate laws. Such rate laws accurately determine the so-called surface-controlled reaction kinetics, but they provide limited information about reaction rates in consolidated porous media.

Natural porous media, such as sedimentary rocks and other geological media encountered in subsurface formations, are inherently heterogeneous [10]. They are mixtures of solid matrix and void space, with the latter consisting of interconnected pores of different shapes, volumes, and surface areas. Furthermore, the mineral composition of surfaces may vary from pore to pore. These pore-to-pore heterogeneities, hereafter referred to as pore-scale heterogeneities, can produce variabilities in the transport and reaction processes that take place within a porous medium, and can result in spatial variations in aqueous concentrations and reaction rates. In such heterogeneous systems, the laboratory-measured geochemical reaction kinetics may not be applicable at the scale of intact porous media. Consequently, spatial heterogeneities at scales smaller than the scale of discretization may be important in determining mineral dissolution and precipitation in reactive transport modeling.

Such scaling effects have been termed “non-classical” behavior as they cannot be predicted by existing theories inferred from laboratory systems [11]. They may be among the potential causes of the oft-cited and discussed field-lab discrepancy, namely, the observed order-of-magnitude differences between lab-measured reaction rates and those derived from field measurements [12–16]. In particular, the scaling effect of geochemical reaction kinetics has been observed in several studies. For example, Szecsody et al. [17] observed that for reactions of $\mathrm{Co^{II/III}}$EDTA with Fe oxide-containing sediments, the reaction parameters measured in batch experiments could not be applied directly to describe the reactive transport processes in column experiments, due to the pore-scale heterogeneity in adsorption sites. They found that stochastic modeling efforts that incorporated pore-scale heterogeneity did reproduce the observations. Lichtner and Tartakovsky [18] used volume-averaging methods to upscale the reaction rate constants for quartz dissolution, incorporating the heterogeneity in mineral grain size. They found that, contrary to the usual modeling assumptions, the upscaled effective reaction rate constants varied as a function of time, which is attributed to heterogeneous distribution of grain sizes.

In this work, we present a methodology to explore upscaling of geochemical reaction kinetics using pore-scale network modeling. A pore-scale network model is one that discretizes the void space of a porous medium into a collection of pores within an interconnected network. Such models have been widely used to explore a variety of phenomena related to multiphase flow in porous media [19–21], including, for example, drying processes [22–25], moisture transport [26], and bubble transport [27]. In recent years, pore-scale network models have also been applied to examine problems concerning chemical and biological processes, such as dissolution of organic liquids [28–32], biomass growth [33–38], adsorption [39,40], and the formation of wormholes in porous media [41]. However, this approach has never been used to address scaling questions associated with geochemical reaction kinetics. As such, this work presents a novel application of pore-scale network modeling.

Within the pore network constructed for this work, the individual pores are considered to be homogeneous systems. Reactive transport processes are simulated at the pore scale, incorporating variations in chemical and physical properties from pore to pore. Using mass balance principles, the continuum-scale reaction rates are obtained from the network model and are compared to continuum-scale rates calculated by ignoring pore-scale details and using laboratory-measured reaction kinetics directly. In addition, we use volume-averaging principles to quantify the errors that may occur when field measured concentrations are used in inverse modeling. The differences between these continuum-scale rates quantify the scaling effect of geochemical reaction kinetics.

This work focuses on the reaction kinetics of minerals that are considered to be important in the context of geological sequestration of CO_2. In geological sequestration, CO_2 is injected into deep subsurface formations and trapped by a variety of mechanisms [42–44]. Studies have found that, for both geological sequestration and natural long-term regulation of atmospheric CO_2 levels, Ca- and Mg-rich feldspars provide the primary sinks for the net consumption of CO_2 [45–51]. In this work, we focus on a Ca-rich feldspar, anorthite, as the model mineral, with kaolinite as the coexisting reactive mineral. The reactions of interest are those that would occur under the acidic conditions created when CO_2 dissolves in formation waters under high pressures. The reaction system is an idealized case from the geochemical point of view, but one which is illustrative in that it makes use of the typical nonlinear rates and equilibrium expressions. Application of the pore-scale network model is demonstrated by upscaling reaction kinetics of anorthite and kaolinite under simulation scenarios that are relevant to geological CO_2 sequestration.

In the remainder of this paper, we first present the laboratory-measured reaction rate laws for anorthite and kaolinite. The methodology to simulate reactive transport processes at the pore scale is then described, followed by construction of the network model. After that we discuss the methodology to calculate the continuum-scale reaction rates. Two simulation scenarios relevant to CO_2 sequestration are then described: one involving high acidity and one involving moderate acidity. Finally, we present the simulation results, explain the reasons for the observed scaling effects, and discuss their implications for reactive transport modeling.

2. The reaction rate laws

2.1. Theory of reaction rate laws

Reaction rate laws are functions that relate mineral dissolution and precipitation rates to the concentrations of aqueous species involved in the reactions (although some rate laws have been described as functions of concentrations of sorbed species [52,53]). Based on transition state theory and the principle of detailed balancing, reaction rate laws take the following general nonlinear form [9]:

$$r = k\prod_{s}\{s\}^{n_s} f(\Delta G), \tag{1}$$

where r is the reaction rate (mol cm^{-2} s^{-1}); k is the reaction rate constant; s represents a chemical species that has catalytic or prohibitory effects on the reaction; $\{s\}$ denotes the activity of species s, the product of the activity coefficient and the aqueous concentration $[s]$; and n_s is a constant that describes the degree of rate dependence on $\{s\}$. The saturation state function $f(\Delta G)$ captures the dependence on the activities of chemical species that directly participate in the reaction.

For the expression of $f(\Delta G)$, the following practical form is used in this work [9]:

$$f(\Delta G) = 1 - \Omega^m, \tag{2}$$

where Ω is the saturation state, and m is a constant that describes the dependence of rate on saturation state. The magnitude of the saturation state Ω is an indicator of how far away the reaction is from equilibrium. Theoretically, it is equal to the ratio of the ionic activity product, IAP, to the equilibrium constant, K_{eq}. As the value of Ω usually covers orders of magnitude, the saturation index, $SI = \log\Omega$, is often used to quantify the magnitude of the saturation state. If $\Omega < 1$, then $SI < 0$, and the net reaction is dissolution; otherwise, the net reaction is precipitation. If $\Omega = 1$ and $SI = 0$, the reaction is at equilibrium.

Mineral dissolution and precipitation reactions are generally driven by several different parallel mechanisms, with each catalyzed by a different chemical species, for instance, H^+, H_2O, and OH^-. The rate law for each mechanism takes the same general form as in Eq. (1):

$$r_H = k_H\{H^+\}^{n_H}(1 - \Omega^m), \tag{3}$$

$$r_{H_2O} = k_{H_2O}(1 - \Omega^m), \tag{4}$$

$$r_{OH} = k_{OH}\{OH^-\}^{n_{OH}}(1 - \Omega^m). \tag{5}$$

The total reaction rate is the sum of these three:

$$r = r_H + r_{H_2O} + r_{OH}. \tag{6}$$

The value of r_H dominates under acidic conditions, and r_{OH} dominates under alkaline conditions. There may or may not be neutral conditions where the rate is dominated by r_{H_2O}, depending on the relative magnitude of these rates. The full reaction rate law requires the following kinetic parameters: the reaction rate constants, k_H, k_{H_2O} and k_{OH}; the degrees of rate dependence on pH, n_H and n_{OH}; and the degree of dependence on saturation state, m.

2.2. Anorthite and kaolinite reactions

In this section, we review the literature on anorthite and kaolinite reaction rates and establish the rate laws used in the present work. The anorthite reaction is as follows:

$$CaAl_2Si_2O_8(s) + 8H^+ \rightleftharpoons Ca^{2+} + 2Al^{3+} + 2H_4SiO_4.$$

It is well known that under conditions far from equilibrium (i.e., $\Omega \ll 1$), the anorthite dissolution rate depends on proton activity in acidic conditions [54]. Examination of published experimental data of anorthite dissolution kinetics suggests that the degree of dependence, n_H, varies from 1 to 3 [55–57]. In this work, we use kinetic parameters measured by Oelkers and Schott [57], who observed that at 25 °C the reaction order of anorthite dissolution with respect to $\{H^+\}$ is 1.5 under acidic conditions. For neutral conditions, we use the reported value for k_{H_2O} of $10^{-15.6}$ mol cm^{-2} s^{-1} [55]; this value is nearly identical to that reported by Helgeson et al. [58]. For alkaline conditions, we use data from Brady and Walther [56], who observed that the exponent describing rate dependence on $\{OH^-\}$ is 0.33. As anorthite dissolution is thermodynamically favorable in most environments and almost never reaches equilibrium, there are no data on the form of its saturation state function. For completeness we include a saturation state

Table 1
Reaction kinetic parameters at 25 °C

	$\log k$ (mol cm^{-2} s^{-1})			n_H	n_{OH}	m	E_a (kJ mol^{-1})
	$\log k_H$	$\log k_{H_2O}$	$\log k_{OH}$				
Anorthite	−7.32[a]	−15.6[b]	−17.5[c]	1.5[a]	0.33[c]	1.0	−18.4[a]
Kaolinite	−14.8[d]	–	−19.7[e]	0.4[d]	0.3[e]	0.9[f]	−29.3[d]

[a] Data from Oelkers and Schott [57], based on measurements for pH 2.4–3.2.
[b] Data from Amrhein and Suarez [55] and Helgeson et al. [58], based on measurements for pH 5–9.
[c] Data from Brady and Walther [56], based on compiled data from various measurements for pH 7–12.
[d] Data from Ganor et al. [59], based on measurements for pH 2–4.2.
[e] Data from Carrol and Walther [60], based on measurements for pH 7–12.
[f] Data from Nagy et al. [61], based on measurements for pH around 3.

function, and use Eq. (2), assuming $m = 1$. Combining all these parameters (summarized in Table 1), the anorthite reaction rate law takes the following form:

$$r_A = (k_H\{H^+\}^{1.5} + k_{H_2O} + k_{OH}\{OH^-\}^{0.33})(1 - \Omega_A), \quad (7)$$

with the expression for the saturation state for the anorthite reaction as follows:

$$\Omega_A = \frac{\{Ca^{2+}\}\{Al^{3+}\}^2\{H_4SiO_4\}^2}{\{H^+\}^8 K_{eq,A}}, \quad (8)$$

where $K_{eq,A}$ is the equilibrium constant of anorthite reaction.

The kaolinite reaction is

$$Al_2Si_2O_5(OH)_4(s) + 6H^+ \rightleftharpoons 2Al^{3+} + 2H_4SiO_4 + H_2O.$$

Examination of kinetics for kaolinite dissolution far from equilibrium reveals that the kaolinite reaction rate does not have an obvious pH-independent region [60]. Under acidic conditions, the kaolinite dissolution rate is reported to be proportional to $\{H^+\}$ raised to the power of 0.35–0.40 [59,60]. In this work, a value of 0.4 is used, based on data from Ganor et al. [59]. The literature on the kaolinite dissolution rate under alkaline conditions suggests that the rate dependence on $\{OH^-\}$ is approximately 0.3 [60], which is the value used in this work. Using the saturation state function from Nagy et al. [61] and assuming that the principle of detailed balancing applies, the overall reaction rate law of kaolinite is as follows:

$$r_K = (k_H\{H^+\}^{0.4} + k_{OH}\{OH^-\}^{0.3})(1 - \Omega_K^{0.9}), \quad (9)$$

with the following expression for the saturation state for kaolinite reaction:

$$\Omega_K = \frac{\{Al^{3+}\}^2\{H_4SiO_4\}^2}{\{H^+\}^6 K_{eq,K}}, \quad (10)$$

where $K_{eq,K}$ is the kaolinite dissolution reaction equilibrium constant. The values of all the kinetic parameters are listed in Table 1. The thermodynamic parameters are discussed in Section 5.

The dissolution rates of both minerals as a function of pH at conditions far from equilibrium are shown in Fig. 1. Of these two reactions, anorthite dissolution has the larger magnitude, leading to the fast release of Ca^{2+}, Al^{3+}, and H_4SiO_4. As a result, in a system where these two minerals coexist, the net reaction of kaolinite is mainly precipitation, consuming the Al^{3+} and H_4SiO_4 released by anorthite dissolution.

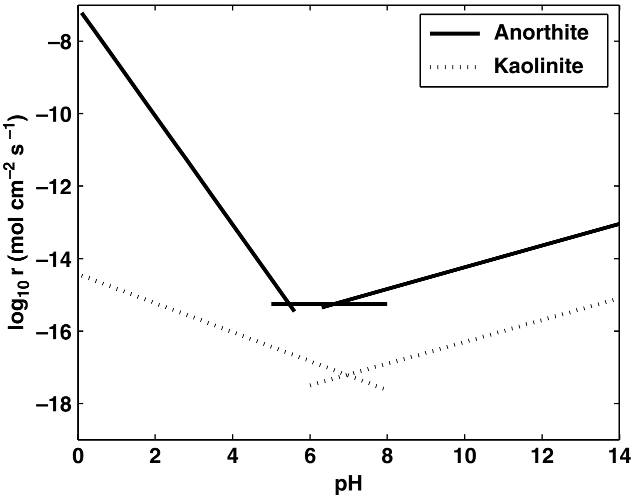

Fig. 1. Dissolution rates of anorthite and kaolinite as a function of pH under conditions far from equilibrium using the parameters summarized in Table 1.

3. Pore-scale network modeling

In pore-scale network modeling, the processes of interest are simulated in individual pores, and information at the pore scale is summed up and averaged over the network to obtain descriptions of processes at the continuum scale. In this way a pore-scale network model serves as a computational tool to upscale processes from the pore scale to the continuum scale. This section presents (i) the equations for reaction and transport at the pore scale, (ii) the construction of the pore network, including parameter specification for porous medium properties, and (iii) the method for flow field calculation.

3.1. Reactive transport processes at the pore scale

Within each pore, the mass of each species in the aqueous phase changes due to transport (advection and diffusion) and reaction processes. The relevant reactions include aqueous reactions, which are considered to be instantaneous, and mineral dissolution and precipitation reactions, which are described kinetically. Examination of different aqueous reactions have shown that there are nine important instantaneous reactions, including the water dissociation reaction, and the speciation reactions of carbon-bearing species, silica-bearing species, and aluminum-bearing species. The two kinetic reactions include the dissolution and precipitation of anorthite and kaolinite. All reactions and their equilibrium constants are listed in Table 2. In total 14 aqueous species are involved in these reactions: Ca^{2+}; H^+; OH^-; the carbon-bearing species $H_2CO_3^*$, HCO_3^-, CO_3^{2-}; the silica-bearing species H_4SiO_4, $H_3SiO_4^-$, $H_2SiO_4^{2-}$; and the aluminum-containing species Al^{3+}, $Al(OH)^{2+}$, $Al(OH)_2^+$, $Al(OH)_3$, $Al(OH)_4^-$.

The aqueous concentrations are assumed to be spatially uniform on the scale of an individual pore. This assumption is justified by the calculation of a Damkohler number, a dimensionless number which compares the relative rates of reaction and transport [62,1]. In this context, the Damkohler number is defined as the ratio of the mineral surface reaction rate to the molecular diffusion rate in an average pore. The fastest reaction of concern is anorthite dissolution under the most acidic condition. The reaction rate is calculated as the product of the area-normalized reaction rate and the average anorthite surface area ($3.0\times10^{-2}\,\mathrm{cm}^2$). At pH $=2.9$ the area-normalized anorthite dissolution rate using Eq. (7) is $10^{-11.6}\,\mathrm{mol\,cm^{-2}\,s^{-1}}$ so the average anorthite dissolution rate is on the order of $10^{-13.3}\,\mathrm{mol\,s^{-1}}$ per pore. The diffusion rate is estimated using the expression $D\times A_c\times\frac{\Delta C}{l}$, with D being the diffusion coefficient (approximately $10^{-4}\,\mathrm{cm^{-2}\,s^{-1}}$ for hydrogen ion [9]), l being the length of the pore (0.017 cm), A_c being the characteristic cross-sectional area for diffusion in a pore, conservatively estimated as l^2, and ΔC ($\mathrm{mol\,cm^{-3}}$) being the difference in concentrations at the center of the pore and at locations close to the mineral surface. For hydrogen ion, ΔC is approximately $10^{-5.9}\,\mathrm{mol\,cm^{-3}}$ at pH of 2.9, which leads to the diffusion rate of $10^{-11.6}\,\mathrm{mol\,s^{-1}}$. This rate is approximately 1.7 orders of magnitude larger than the reaction rate. This relatively fast diffusion rate, combined with the much faster advection rate, is sufficient to eliminate the concentration gradient within the fluid in individual pores.

The mass balance equations describing the mass change of chemical species within individual pores were developed following Lichtner's systematic formulation for multicomponent systems that involve both kinetically controlled and instantaneous reactions [63,64]. We chose to develop the mass balance equations for five key components: Ca^{2+}, C_T, Si_T, Al_T, and H_T, with C_T collectively representing all carbon-bearing species, Si_T collectively representing all silica-bearing species, Al_T collectively representing all aluminum-bearing species, and H_T representing the total aqueous proton. The concentration of H_T is computed as $[H_T]=-[Al(OH)^{2+}]-2[Al(OH)_2^+]-3[Al(OH)_3]-4[Al(OH)_4^-]+[H_4SiO_4]-[H_2SiO_4^{2-}]+[H_2CO_3^*]-[CO_3^{2-}]+[H^+]-[OH^-]$. For this system, five mass balance equations, together with the nine mass action laws corresponding to the nine instantaneous reactions, are sufficient to describe the mass change in the aqueous phase.

The mass balance equation (expressed in molar units) for pore i takes the following general form:

$$V_i\frac{\mathrm{d}[\cdot]_i}{\mathrm{d}t}=\sum_{Q_{ij}>0}Q_{ij}[\cdot]_j+\sum_{Q_{ij}<0}Q_{ij}[\cdot]_i+\sum_{j=1}^{\mathrm{nc}}D^*_{ij,\cdot}a_{ij}\frac{([\cdot]_j-[\cdot]_i)}{l}+S_{i,\cdot}, \tag{11}$$

where $[\cdot]$ represents the molar concentration of one of the five key components; V_i is the volume of pore i; j is the index for a pore that is connected to pore i; nc

Table 2
Reactions of interest, and their equilibrium constants adjusted to current simulation conditions (50 °C and 10^7 Pa)

	Reactions	$\log K_{eq}$[a]
Kinetic reactions	$CaAl_2Si_2O_8(s)+8H^+\rightleftharpoons Ca^{2+}+2Al^{3+}+2H_4SiO_4$	21.7
	$Al_2Si_2O_5(OH)_4(s)+6H^+\rightleftharpoons 2Al^{3+}+2H_4SiO_4+H_2O$	3.80
Instantaneous reactions	$H_2O\rightleftharpoons H^++OH^-$	−13.2
	$H_2CO_3^*\rightleftharpoons HCO_3^-+H^+$	−6.15
	$HCO_3^-\rightleftharpoons CO_3^{2-}+H^+$	−10.0
	$H_4SiO_4\rightleftharpoons H_3SiO_4^-+H^+$	−9.2
	$H_3SiO_4^-\rightleftharpoons H_2SiO_4^{2-}+H^+$	−12.4
	$Al^{3+}+OH^-\rightleftharpoons Al(OH)^{2+}$	8.76
	$Al(OH)^{2+}+OH^-\rightleftharpoons Al(OH)_2^+$	18.9
	$Al(OH)_2^++OH^-\rightleftharpoons Al(OH)_3$	27.3
	$Al(OH)_3+OH^-\rightleftharpoons Al(OH)_4^-$	33.2

[a] The method of adjustment is described in Section 5.

is the total number of neighbor pores; Q_{ij} symbolizes the flow rate from pore j to i; $D^*_{ij,\cdot}$ is the effective diffusion coefficient; a_{ij} is the cross-sectional area between pores i and j; l is the distance between the centroids of adjacent pores and is a constant for the regular-latticed network; and $S_{i,\cdot}$ denotes the mass change rate due to kinetic reactions. On the right-hand side of the above equations, the first two terms take into account advective mass inflow and outflow rates, and the third term is the mass change rate due to diffusion between adjacent pores.

For each of the four components that is a collective representation of several species, its "effective" diffusion coefficient $D^*_{ij,\cdot}$ is derived by writing the reactive transport equations for each constitutive species. Summation of these transport equations leads to a derived effective diffusion coefficient that is essentially a weighted average of the diffusion coefficients of involved species weighted by their concentration differences between pore i and pore j. Such a formulation is consistent with what is done in reactive transport modeling [64]. For example, for C_T,

$$D^*_{ij,C_T} = \frac{D_{H_2CO_3^*}([H_2CO_3^*]_j - [H_2CO_3^*]_i) + D_{HCO_3^-}([HCO_3^-]_j - [HCO_3^-]_i) + D_{CO_3^{2-}}([CO_3^{2-}]_j - [CO_3^{2-}]_i)}{([H_2CO_3^*]_j - [H_2CO_3^*]_i) + ([HCO_3^-]_j - [HCO_3^-]_i) + ([CO_3^{2-}]_j - [CO_3^{2-}]_i)}. \tag{12}$$

The diffusion coefficients for individual species are taken from the literature [65,9]. Note that this formulation of mass balance equations leads to continuum-scale dispersion effects by taking into account fluctuations in local flow velocities. Hence, dispersion is not modeled explicitly and the diffusion process is restricted to pore-to-pore diffusion within the network.

The last term in Eq. (11), $S_{i,\cdot}$, represents the mass change rate due to kinetic reactions. It takes different forms for different components, depending on the reactions involved (expressed in molar units):

$$S_{i,Ca^{2+}} = r_{A,i}\mathscr{A}_{A,i}, \tag{13}$$

$$S_{i,C_T} = 0, \tag{14}$$

$$S_{i,Si_T} = 2r_{A,i}\mathscr{A}_{A,i} + 2r_{K,i}\mathscr{A}_{K,i}, \tag{15}$$

$$S_{i,Al_T} = 2r_{A,i}\mathscr{A}_{A,i} + 2r_{K,i}\mathscr{A}_{K,i}, \tag{16}$$

$$S_{i,H_T} = -6r_{A,i}\mathscr{A}_{A,i} - 4r_{K,i}\mathscr{A}_{K,i}, \tag{17}$$

where $\mathscr{A}_{A,i}$ and $\mathscr{A}_{K,i}$ are, respectively, the surface areas of anorthite and kaolinite in pore i. The two reaction rates, $r_{A,i}$ and $r_{K,i}$, are calculated using the respective reaction rate laws (Eqs. (7) and (9)) and the local concentrations in pore i. The mass change rates due to kinetic reactions depend on the amount of the reactive mineral in each pore. In this pore network model, two types of pores are identified with regard to the mineralogy of the solid phases: reactive pores, with their solid phases containing both anorthite and kaolinite, and non-reactive pores, with their solid phases being quartz. For non-reactive pores, as the reactive minerals are not present, the surface areas of anorthite and kaolinite are zero and the mass change rates due to reaction are equal to zero.

Such a representation of reactive pores is not a problem for modeling dissolution, but could pose a problem for modeling precipitation. Precipitation normally proceeds in two steps: nucleation and crystal growth [9,66]. For many minerals, nucleation is the rate-limiting step [43], because it has to overcome a surface free energy barrier and requires some degree of supersaturation. In the absence of a solid mineral phase, precipitation of that mineral requires both steps, while in the presence of a solid mineral phase, precipitation of that mineral can start as crystal growth. The large difference in these rates is the basis for our modeling assumption that precipitation can proceed only in so-called reactive pores.

3.2. Network construction

A 3D regular-lattice network model was constructed to represent a consolidated sandstone with reactive minerals occupying approximately 10% of the solid phase, which is within the typical range of the percentage of feldspars and clay minerals in sandstones. The porosity of the network is 0.14, and the permeability is $7.9 \times 10^{-10}\,\text{cm}^2$, which falls in the typical range of consolidated sandstone properties [67,68]. The size of the network is $5.0 \times 1.7 \times 5.0\,\text{mm}^3$, and the network contains 9000 pores ($30 \times 10 \times 30$ in x-, y-, z-directions, respectively). The bulk flow direction is in the z-direction. This network has several characteristics that distinguish it from network models that have been constructed for multiphase flow. First, pores do not have prescribed geometries; they are defined only in terms of surface area and volume. Second, pore throats are not represented explicitly except to assign an effective resistance to the flow and an effective cross-sectional area for diffusion. All void volume is contained in pore bodies.

Solution of the pore-scale mass balance equations requires the following values for each pore i: volume; conductances at pore junctions (for the calculation of flow rates); effective cross-sectional areas at connections of adjacent pores (for the calculation of diffusion terms); and surface areas. These parameters characterize each pore, while across the network they form statistical distributions. The parameters for each pore are randomly assigned from their respective statistical distributions, as discussed in this section.

3.2.1. Pore volume

Based on literature data for a Fontainebleau sandstone [69], pore volume is assumed to have a log-normal distribution. The mean for the log-transformed pore volume (mm^3) is -3.42, with the standard deviation of the log-transformed pore volume being 0.51. This corresponds to an arithmetic mean of pore volume being $6.6 \times 10^{-4}\ \mathrm{mm}^3$.

3.2.2. Pore hydraulic conductance

For the distribution of pore conductances, we have made two assumptions: (1) the distribution follows a log-normal distribution; and (2) the conductance between pores is correlated to the sum of the logarithm of their pore volumes. Regarding the first assumption, although data on distributions of pore-scale conductances generally do not exist, in the literature there is indirect evidence supporting the idea that the distribution of the conductances should be related to the distribution of grain or pore size, which is usually log-normally distributed [70]. The second assumption is based on observations for sandstones from experimental studies [71,72].

We define C_{ij} ($\mathrm{cm}^4\,\mathrm{g}\,\mathrm{Pa}^{-1}$) as the conductance between two adjacent pores i and j. The log-transformed conductance $X_{ij} = \ln C_{ij}$ has a normal distribution, with mean μ_X, and variance σ_X^2. The summation of the log-transformed volumes of adjacent pores, $Y_{ij} = \ln V_i + \ln V_j$, also takes a normal distribution, with mean $\mu_Y = 2\mu_{\ln V}$ and variance $\sigma_Y^2 = 2\sigma_{\ln V}^2$. Assuming X_{ij} and Y_{ij} are jointly Gaussian distributed, the mean and variance of the log-transformed conductance for a pair of connected pores i and j, $(\mu_X)_{ij}$ and $(\sigma_X^2)_{ij}$, are calculated as follows [73]:

$$(\mu_X)_{ij} = \mu_X + \rho \frac{\sigma_X}{\sigma_Y}(Y_{ij} - \mu_Y), \tag{18}$$

$$(\sigma_X^2)_{ij} = \sigma_X^2(1.0 - \rho^2), \tag{19}$$

where ρ is the correlation coefficient. For the connection between pores i and j, the conductance is sampled from the log-normal distribution with mean $(\mu_X)_{ij}$ and variance $(\sigma_X^2)_{ij}$, which depend on the log-volume summation Y_{ij}. In this work, the value of μ_X and σ_X^2 were chosen to be -6.1 and 1.0 to be consistent with the permeability value ($7.9 \times 10^{-10}\ \mathrm{cm}^2$), as described in the next section. The value of ρ is assumed to be 0.9 as we assume strong correlation between conductance and adjacent pore volumes.

3.2.3. Pore-to-pore cross-sectional area

The cross-sectional area between connected pores i and j, a_{ij}, is required for the calculation of the mass transport due to diffusion. Considering an "effective" cylinder between pore i and j, with conductance C_{ij}, and length l, the diameter of the cylinder d_{ij} can be calculated by rearranging Poiseuille's law:

$$d_{ij} = \left(\frac{128 v l \times C_{ij}}{\pi}\right)^{\frac{1}{4}}, \tag{20}$$

with v being the viscosity of the flowing fluid. Correspondingly, the "effective" cross-sectional area $a_{ij} = \frac{1}{4}\pi d_{ij}^2$. The arithmetic average of the cross-sectional area for this network is about $1.02 \times 10^{-4}\ \mathrm{mm}^2$.

3.2.4. Surface area

Because there is no reliable literature data on the pore-scale distribution of surface area for consolidated sandstone, we use the following procedure. The surface area of pore i is randomly sampled from an exponential distribution, with the restriction of not being less than the minimum surface area, which is calculated from the pore volume assuming a spherical pore. The values of surface areas of consolidated sandstones measured by Brunauer–Emmet–Teller (BET) method, often reported as the surface-to-volume ratio, cover three orders of magnitude, ranging from 10^3 to $10^5\ \mathrm{cm}^{-1}$ [74–76]. In this work, the mean of the pore surface area was chosen to be $6.0\ \mathrm{mm}^2$, which results in a surface-to-volume ratio for the entire network of $1.3 \times 10^4\ \mathrm{cm}^{-1}$.

As described earlier, the solid surface for an individual pore is modeled as either containing reactive minerals or not. Within 9000 pores in total, 900 of them contain reactive minerals, which is consistent with the assumption that 10% of the solid phase is reactive mineral. We have chosen to randomly distribute the reactive minerals in clusters of size $2 \times 2 \times 15$ pores (in the x-, y-, z-directions, respectively), which is within the range of the spatial scale of feldspars distribution in sandstone [77]. In pores within the reactive clusters, 50% of the surface area is anorthite and 50% is kaolinite. The resulting distributions of values of $\mathscr{A}_{\mathrm{A},i}$ and $\mathscr{A}_{\mathrm{K},i}$ for the network include a large number of zeros for the non-reactive pores and a truncated exponential distribution for the surface areas in reactive pores.

3.3. Determination of the steady-state flow field

To determine the steady-state flow field of the network, fixed fluid pressures are imposed at the boundaries of the network in the z-direction, with no-flow boundary conditions applied in the other two directions, resulting in macroscopically one-dimensional flow. The flow rate between connected pores i and j is proportional to the pressure difference through the conductance:

$$Q_{ij} = C_{ij}(P_i - P_j), \tag{21}$$

where P_i and P_j are fluid pressures in pore i and j, respectively. The inflows and outflows must balance for each pore i:

$$\sum_{j=1}^{\mathrm{nc}} Q_{ij} = 0. \tag{22}$$

Combination of Eqs. (21) and (22) results in a linear algebraic system for the unknown pressure field. Given the boundary pressures, this system is solved for the pressure in each pore, from which the steady-state flow field is calculated.

At the continuum scale, the total flow rate follows Darcy's law:

$$Q_{\mathrm{T}} = \frac{\kappa}{\nu} \Lambda \frac{\Delta P}{L}, \tag{23}$$

where Q_{T} ($\mathrm{cm}^3\ \mathrm{s}^{-1}$) denotes the total flow rate through the network in the main flow direction, z; κ is the intrinsic permeability of the network (cm^2); Λ represents the cross-sectional area of the network in the direction orthogonal to the main flow (cm^2); ΔP symbolizes the pressure difference between the two boundaries in z-direction; and L is the length of the network in z-direction (cm). By rearrangement of the above equation, the permeability of the network can be calculated. The permeability is thus a function of the mean and variance of the conductance field, μ_X and σ_X^2, and the correlation with local volumes. As mentioned previously, these parameters were chosen so that the permeability corresponds to a typical value for sandstone. An iterative approach was used whereby the statistical parameters were varied until a flow field was generated that resulted in the desired permeability.

4. Continuum-scale reaction rates

4.1. The rates from the network model: $\boldsymbol{R}_N$

For a porous medium, the "true" reaction rate at the continuum scale is the total mass change rate due to reactions at every reactive surface, normalized by the total amount of surface area of reactive minerals. The network model allows us to estimate such a "true" reaction rate at the continuum scale. The pore-scale mass balance equations are used to simulate changes in aqueous concentration over time in each pore. At each time step, the sum of the mass change rates due to mineral reactions for the entire network, divided by the total surface area of reactive minerals, gives the "true" reaction rate for the network. For example, for anorthite, the effective continuum-scale reaction rate for the network model is as follows:

$$R_{\mathrm{N,A}} = \frac{\sum_{i=1}^{n} \mathscr{A}_{\mathrm{A},i} r_{\mathrm{A},i}}{\sum_{i=1}^{n} \mathscr{A}_{\mathrm{A},i}}, \tag{24}$$

where n is the total number of pores. Expressed in $\mathrm{mol\ cm}^{-2}\ \mathrm{s}^{-1}$, this rate is equivalent to the rate calculated by summing the mass change rate of Ca^{2+} due to anorthite reaction across the network, and then dividing by the total anorthite surface area. An equation analogous to Eq. (24) is used to calculate the continuum-scale rate for kaolinite. The continuum-scale rates, $R_{\mathrm{N,A}}$ and $R_{\mathrm{N,K}}$, depend on local reaction rates ($r_{\mathrm{A},i}$ and $r_{\mathrm{K},i}$, respectively), as well as the coupling between the local rates and local surface area of reactive minerals. For non-reactive pores, as values of $\mathscr{A}_{\mathrm{A},i}$ are zero, the term $\mathscr{A}_{\mathrm{A},i} r_{\mathrm{A},i}$ is not counted in the calculation of R_{N}. As such, concentrations in non-reactive pores are irrelevant to the reaction rates, although they enter indirectly via the transport equations. The continuum-scale reaction rates are dependent only on the concentrations in reactive pores.

4.2. The rates from the continuum model: R_C

This section presents the methodology for calculating continuum-scale reaction rates using a continuum model, which is the fundamental building block of traditional forward modeling. Forward modeling generally employs a continuum approach [63,64,78], in which porous media are characterized by spatially-averaged properties at the scale of the grid block, thereby ignoring details at the sub-grid scale. It is common practice to apply reaction rate laws determined from well-mixed laboratory systems to calculate the reaction rates for the porous medium in an entire grid block. Furthermore,the mathematical forms and parameters of these rate laws are assumed to hold at the grid block scale despite possible nonlinearities in upscaling.

In a similar manner, the continuum model uses spatially-averaged values to represent system properties, assumes uniform concentrations in the aqueous phase, and applies lab-measured reaction rates directly at the continuum scale. In so doing, it ignores pore-scale heterogeneities a priori, and assumes no mass transport limitation from pore to pore. In the calculation that follows, the continuum model is constrained to have the same hydrodynamic properties, total surface area of reactive minerals, initial conditions and boundary conditions as the network model.

Because the reactions and the species involved are the same as in the network model, we follow the same systematic formulation to develop mass balance equations for the five components: Ca^{2+}, $\mathrm{C_T}$, $\mathrm{Si_T}$, $\mathrm{Al_T}$, and $\mathrm{H_T}$. For each key component, the mass balance equations take the following general form, applied over the entire volume of the pore network defined earlier:

$$V_{\mathrm{T}} \frac{\mathrm{d}[\cdot]}{\mathrm{d}t} = Q_{\mathrm{T}}[\cdot]_{\mathrm{in}} - Q_{\mathrm{T}}[\cdot]_{\mathrm{C}} + S_{\mathrm{C},\cdot}, \tag{25}$$

where V_T is the total pore volume across the network, $[\cdot]_{in}$ corresponds to the concentration at the inflow boundary, and $[\cdot]_C$ is the uniform concentration in the continuum model. On the right side of the equation, the first two terms account for the mass change rates due to advection, and the last term, $S_{C,\cdot}$, represents the mass change rate due to reaction, which takes different forms for different components:

$$S_{C,Ca^{2+}} = R_{C,A}\mathscr{A}_{A,T}, \tag{26}$$

$$S_{C,C_T} = 0, \tag{27}$$

$$S_{C,Si_T} = 2R_{C,A}\mathscr{A}_{A,T} + 2R_{C,K}\mathscr{A}_{K,T}, \tag{28}$$

$$S_{C,Al_T} = 2R_{C,A}\mathscr{A}_{A,T} + 2R_{C,K}\mathscr{A}_{K,T}, \tag{29}$$

$$S_{C,H_T} = -6R_{C,A}\mathscr{A}_{A,T} - 4R_{C,K}\mathscr{A}_{K,T}, \tag{30}$$

where $R_{C,A}$ and $R_{C,K}$ are the reaction rates of anorthite and kaolinite, respectively, and $\mathscr{A}_{A,T}$ and $\mathscr{A}_{K,T}$ are the total surface areas of anorthite and kaolinite. These mass balance equations look similar to those written for an individual pore in the network model, except that at the continuum scale there is no diffusion term, and the parameters characterizing pore i are replaced by the parameters that describe the continuum-scale properties. The reaction rates from the continuum model, $R_{C,A}$ and $R_{C,K}$, are calculated using the uniform concentrations (converted to activities), and by applying the reaction rate laws directly. For anorthite,

$$R_{C,A} = (k_H\{H^+\}_C^{1.5} + k_{H_2O} + k_{OH}\{OH^-\}_C^{0.33})(1 - \Omega_{C,A}), \tag{31}$$

where $\Omega_{C,A}$ is calculated using uniform concentrations as well. For kaolinite, the rate expression is similar, following the reaction rate law shown in Eqs. (9) and (10). These rates represent the rates calculated in one grid block in forward modeling, where the grid block is taken to correspond to the entire network used in the network model.

4.3. The rates from volume-averaged concentrations: R'_N

This section presents the methodology for calculating continuum-scale rates, R'_N, using volume-averaged concentrations in reaction rate laws. The volume-averaged concentrations are analogous to those measured in field sampling, where groundwater is pumped from a well, and water from a large number of pores is mixed. Concentrations measured in the sample represent spatially-averaged values. A typical application in inverse modeling is to use these measured concentrations in conjunction with laboratory-measured reaction rate laws or equilibrium relationships to infer which minerals are dissolving, and which are precipitating [79].

The purpose of this calculation is not to develop a method of volume-averaging, but to use the network model to calculate the rates that resemble those estimated from field sampling. This allows us to examine the extent to which volume-averaged concentrations, $\overline{[\cdot]}$, provide accurate predictions of continuum-scale reaction rates. From the network model simulation results, we compute the volume-averaged concentrations, such as that of hydrogen ion, as follows:

$$\overline{[H^+]} = \frac{\sum_{i=1}^{n} V_i[H^+]_i}{\sum_{i=1}^{n} V_i}. \tag{32}$$

Since activity coefficients are constant throughout the network (see Section 5), the value of the volume-averaged activity, $\overline{\{H^+\}}$, is the product of the activity coefficient and the volume-averaged concentration. Then, for the anorthite reaction, we use the averaged activities to compute

$$R'_{N,A} = (k_H\overline{\{H^+\}}^{1.5} + k_{H_2O} + k_{OH}\overline{\{OH^-\}}^{0.33})(1 - \Omega'_{N,A}), \tag{33}$$

where

$$\Omega'_{N,A} = \frac{\overline{\{Ca^{2+}\}}\,\overline{\{Al^{3+}\}}^2\,\overline{\{H_4SiO_4\}}^2}{\overline{\{H^+\}}^8 K_{eq,A}}. \tag{34}$$

A similar rate law applies for kaolinite. In so doing, the rate calculated from volume-averaged concentrations ignores pore-scale heterogeneities a posteriori. These reaction rates represent the rates that would be inferred from the measured concentrations via inverse modeling.

4.4. Comparison between continuum-scale reaction rates

We have defined three continuum-scale reaction rates: (1) R_N, derived from explicit mass balance calculation from the network model; (2) R_C, derived from uniform concentrations in the continuum model; and (3) R'_N, derived from averaged concentrations from the network model. Of these three upscaled reaction rates, we take R_N to represent the "true" reaction rate, as it most closely takes into account the effects of pore-scale heterogeneities, and is consistent with the mass balance of the network system. Both R_C and R'_N are based on spatially-averaged properties (either a priori or a posteriori) and on reaction rate laws that were determined in the laboratory. Comparisons of R_C and R'_N to R_N provide insights into how pore-scale heterogeneity influences continuum-scale reaction rates, and how well the use of average properties represents these heterogeneous systems.

For the comparison of R_C to R_N, we define the ratio:

$$\eta \equiv \frac{R_C}{R_N}. \tag{35}$$

If η is close to unity, the differences between these two rates are not significant, which means that the effects of pore-scale heterogeneities are not significant, and that the scaling effect is negligible. In such cases, the application of the lab-measured reaction kinetics at the continuum scale is appropriate in forward modeling. Otherwise, pore-scale heterogeneities are important and conventional forward modeling using continuum modeling may introduce significant errors.

For the comparison of R'_{N} and R_{N}, we define the ratio:

$$\beta \equiv \frac{R'_{\mathrm{N}}}{R_{\mathrm{N}}}. \tag{36}$$

If β is close to unity, these two rates are similar, which means that volume-averaged concentrations are sufficient to describe the reaction rates and the scaling effect is negligible. Otherwise, it is not appropriate to calculate the reaction rates using volume-averaged concentrations, such as those determined from field sampling and used in inverse modeling.

The deviation of η or β values from unity provides a measure of the scaling effect of the reaction kinetics. If either R_{C} or R'_{N} has a different sign from R_{N}, then R_{C} or R'_{N} predicts a different reaction direction as compared to R_{N}; that is, one is predicting dissolution while the other is predicting precipitation, or other wise.

5. Simulation conditions and numerical computation

5.1. Simulation conditions and parameter estimation

The application of pore-scale network modeling to upscale geochemical reaction rates is illustrated with two simulation scenarios relevant to geological CO_2 sequestration. One scenario is that in which the network system is near the CO_2 injection site so that the boundary aqueous phase is in equilibrium with CO_2 of a typical injection pressure, 10^7 Pa, and is highly acidic (referred to hereafter as case A). The other scenario is that in which the network system is relatively far away from the injection site so that the boundary aqueous phase has a much lower CO_2 concentration. Here, we have chosen to represent this as an aqueous phase in equilibrium with CO_2 of a relatively low pressure, 10^5 Pa (referred to hereafter as case B). The difference in CO_2 concentrations generates different acidities in the aqueous phases that flow into the network system. Except for this difference, the simulation conditions are the same for the two cases.

In geological sequestration, CO_2 would typically be injected into subsurface formations at a depth of 1 km or greater. To be consistent with this depth, the simulations were run at a temperature of 323 K and a pressure of 10^7 Pa. The brine is represented by saline water with total dissolved salinity ($\mathrm{TDS} = 0.45\ \mathrm{mol\ L^{-1}}$) that has taken into account the contribution of all important aqueous species in typical brine. Initially the brine is assumed to be in equilibrium with quartz and kaolinite, at pH 7.5. The electronic condition is satisfied with the addition of Ca^{2+}, which produces an initial concentration that is very small ($7.9 \times 10^{-6}\ \mathrm{mol\ L^{-1}}$). There are no carbon-bearing species present in the brine. The brine at the inflowing boundary is assumed to have the same $[Ca^{2+}]$ as in the initial aqueous phase within the network. The total carbon concentration and thus the pH in the boundary brine is determined using the semi-empirical relationship from Duan and Sun [80], based on equilibrium with separate phase carbon dioxide at a given temperature, pressure, and salinity. In case A, due to the large amount of CO_2 dissolved in the boundary brine, the boundary pH is 2.9. In case B, the boundary pH is 4.1. We chose to run the simulations for a nominal value using the flow velocity, $q = 5.8 \times 10^{-3}\ \mathrm{cm\ s^{-1}}$ [67].

The salinity is high enough that the activity coefficients of the reactive species deviate considerably from unity. These values were calculated using the Davies equation [81]. Because the brine TDS is high, it is assumed that the dissolution and precipitation of reactive species does not change the TDS significantly, and the activity coefficient of each species is considered constant both in time and space.

Equilibrium constants were taken from Morel and Hering [81] and adjusted to the system temperature and pressure using the software SUPCRT92 [82], as listed in Table 2. The reaction rate constants were adjusted to the given temperature using the Arrhenius equation [9], with the activation energies listed in Table 1. The diffusion coefficients were obtained and adjusted to the system temperature and salinity [9,65]. The effects of pressure on reaction rate constants and diffusion coefficients were considered insignificant, because the pressure effect on these parameters is relatively small compared to the effect of temperature [9].

Simulations were run within a limited time frame such that the total amount of minerals reacted produced only small porosity changes. Using empirical relationships between permeability and porosity [83–85], the predicted porosity changes result in changes of permeability less than 5%. Therefore, the porosity and permeability of the porous medium are considered constant during the simulation process. The system eventually reaches steady state, after which the concentrations of the aqueous species and the reaction rates do not vary as a function of time.

5.2. Numerical computations

For the network model, given initial and boundary conditions, as well as the predetermined flow field, we use the adaptive Runge–Kutta algorithm to simultaneously solve the mass balance equations for the concentrations of the five components in each pore at each time step [86]. The values of these five concentrations, coupled with the nine laws of mass action corresponding to the nine instantaneous reactions, are then used to calculate concentrations of all 14 species iteratively using a hybrid algorithm combining both the Newton–Raphson and bisection method. In this way we obtain the concentrations of all 14 aqueous species in each pore at each time step. The concentrations of the aqueous species in the continuum model are solved in the same way.

6. Results

In this section, we first present the results on the pore-scale heterogeneities of concentrations and reaction rates for case A, then briefly compare the pore-scale heterogeneities in case A and case B. After that, the evolution of the continuum-scale reaction rates are described, and the scaling effect is examined in the context of continuum modeling and volume-averaging. Finally, the resulting concentrations in the network model are examined with respect to network-scale equilibrium relationships.

6.1. Pore-scale heterogeneities: case A

The locations of reactive pores for two orthogonal planes in the network are shown in Fig. 2. For the simulation conditions of case A, the steady-state concentration fields of log[Ca^{2+}] and pH for the $y = 5$ plane are shown in Fig. 3. In general, the Ca^{2+} concentrations and pH values are lower in pores near the left boundary due to the low calcium content and acidic condition of the inflowing water. As the inflowing water encounters reactive minerals, anorthite slowly dissolves and releases Ca^{2+}. Correspondingly, there is an increase in pH due to the increase in alkalinity. The concentrations of Ca^{2+} and the pH in reactive pores are generally higher than those in nearby non-reactive pores, as indicated by the similar patterns of high-concentration clusters and low pH clusters (Fig. 3), to that of reactive pore clusters (Fig. 2). Non-reactive pores may also have elevated Ca^{2+} concentrations and pH if they are close to reactive pores. For example, near the inflow boundary where x is approximately 17 or 18, the high [Ca^{2+}] and pH are due to the proximity of these pores to the reactive clusters in the $y = 3$ and $y = 4$ layer.

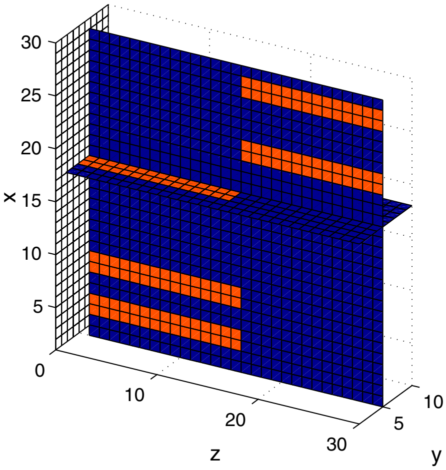

Fig. 2. Locations of reactive pores for the $y = 5$ plane and for the $x = 18$ plane. Reactive pores are shown in red color.

The pore-scale concentrations vary considerably over the network: the values of [Ca^{2+}] cover 2.5 orders of magnitude, and hydrogen ion concentrations cover approximately half an order of magnitude. The frequency

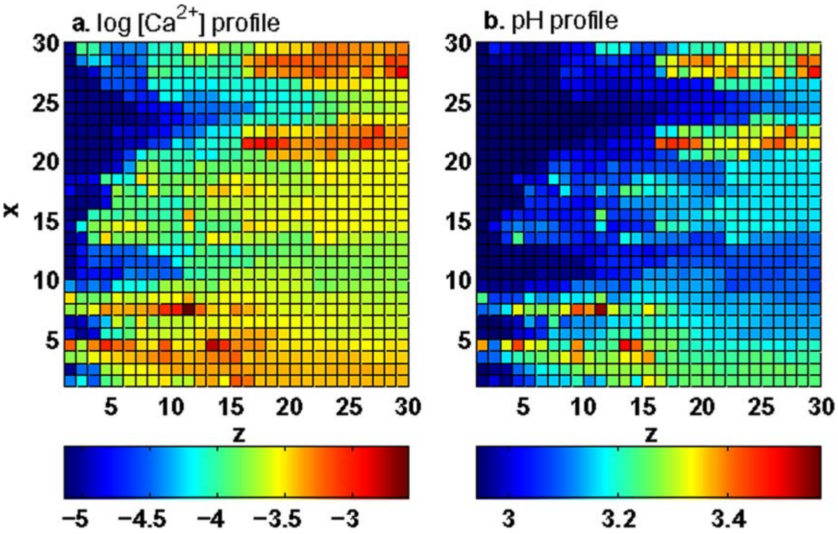

Fig. 3. For one layer of pores in the middle of the network ($y = 5$): steady-state profiles of log[Ca^{2+}] (a) and pH (b). Boundary fluid flows in from the left (at $z = 0$).

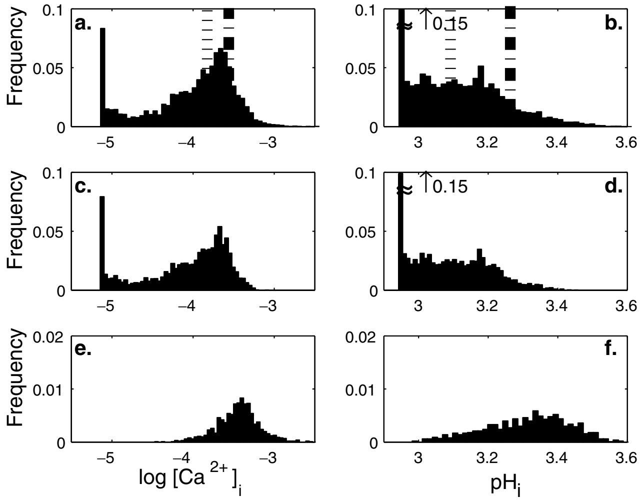

Fig. 4. Steady-state distributions of log[Ca^{2+}] and pH in all pores (a and b); in non-reactive pores (c and d), and in reactive pores (e and f). The dot-dashed lines indicate the uniform concentrations from the continuum model. The dotted lines indicate the volume-averaged concentrations.

distributions of log[Ca^{2+}] and pH for pores in the entire network are shown in Fig. 4a and b. Both distributions are highly skewed. For Ca^{2+}, approximately 9% of the pores have the minimum concentration values, which is equal to that of the inflowing boundary. Similarly, approximately 15% of the pores have the minimum value of pH. Calcium concentration has a bimodal distribution, in which a second peak arises at the large end of the concentration range.

For comparison, the distributions of log[Ca^{2+}] and pH in non-reactive pores are shown in Fig. 4c and d. Because the non-reactive pores occupy 90% of the pores, their concentration distributions bear great similarity to the distributions for all pores, except at the right end of the concentration range, where concentrations in reactive pores play an important role. The distributions of concentrations in reactive pores have very different shapes from those for non-reactive pores, as shown in Fig. 4e and f (Note the different scale of frequency axis). They are less skewed, and have peaks that fall in the large ends of the concentration ranges, indicating the relatively high [Ca^{2+}] and pH in reactive pores.

Also shown in Fig. 4a and b are the logarithm of volume-averaged calcium concentration and the logarithm of volume-averaged hydrogen ion concentration (referred to hereafter as volume-averaged pH), as well as the logarithm of the uniform concentrations calculated from the continuum model. While both volume-averaged concentrations lie in the mid-range of the distributions for the entire network, they fall in the tail region at the low end of the concentration range in reactive pores. For pH, more than 90% of the reactive pores have values larger than the volume-averaged value. The uniform concentrations from the continuum model represent concentrations in reactive pores better, as they are closer to the modes of the concentrations in reactive pores.

Due to the dependence of reaction rates on aqueous concentrations, the pore-scale concentration heterogeneities lead to spatial variations in saturation states, and in reaction rates. Fig. 5 shows the steady-state distributions of saturation indexes (see Section 2.1) and reaction rates for anorthite. The saturation states cover approximately 10 orders of magnitude. However, they are all orders of magnitude smaller than unity, and therefore anorthite dissolution remains far from equilibrium in all pores. As such, anorthite dissolution rates are largely determined by inherent mineral reactivity and the activities of catalytic species. That is, the value of $1 - \Omega_A$ in Eq. (7) is approximately unity. In fact, at steady state, all the pores in the network have acidic pH conditions such that the anorthite dissolution rate in each pore is approximately:

$$r_{A,i} \cong k_H\{H^+\}_i^{1.5}. \tag{37}$$

Thus, spatial variations in anorthite dissolution rates are entirely due to spatial variation in pH in reactive pores. As is consistent with the exponent in Eq. (37), the variance in the logarithm of $r_{A,i}$ is roughly twice that of pH (as expected given that the square of 1.5 is 2.25). The hydrogen ion concentrations span roughly 0.65 orders of magni-

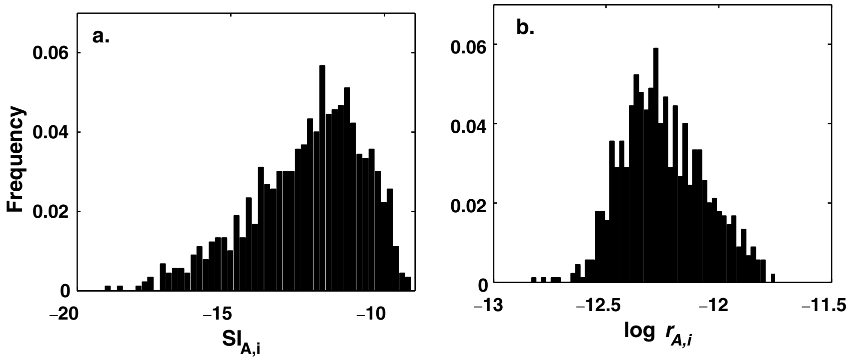

Fig. 5. For anorthite: steady-state distributions of saturation indexes (a) and logarithm of reaction rates (b).

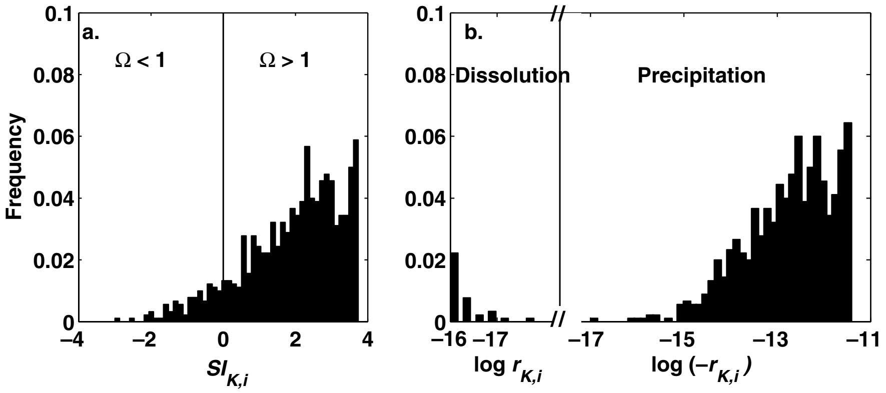

Fig. 6. For kaolinite reaction: steady-state distributions of saturation indexes (a) and logarithm of local reaction rates (b).

tude, and the anorthite dissolution rates cover approximately one order of magnitude, as shown in Fig. 5b.

As shown in Fig. 6, for kaolinite, the saturation indexes include both positive and negative values, indicating that dissolution is occurring in some pores and precipitation is occurring in others. As the values of saturation state are either in a similar order of magnitude as unity, or orders of magnitude larger, the spatial variation of local rates depends not only on pH heterogeneities, but also on concentration heterogeneities of Al^{3+} and H_4SiO_4, with the dependence on $\{H^+\}$ raised to the power of approximately −5.0 (refer to Eqs. (9) and (10)). Such high dependence of rates on concentrations results in large spatial variations in kaolinite reaction rates, as illustrated in Fig. 6b. In about 6% of reactive pores, dissolution occurs and the rates span almost two orders of magnitude; in more than 90% of reactive pores, precipitation occurs, and the rates span approximately 4.6 orders of magnitude. This is an interesting illustration of the effect of pore-scale heterogeneity.

6.2. Comparison of pore-scale heterogeneities for case A and B

Case B is different from case A in that its boundary fluid is much less acidic (with pH of 4.1, compared to 2.9 in case A). Due to the sensitivity of anorthite dissolution rate on hydrogen ion concentration, the reduced acidity results in smaller anorthite dissolution rates, and smaller differences in concentrations between reactive and non-reactive pores. As illustrated by Fig. 7a, the anorthite dissolution rates shift to smaller values, and cover a much narrower range, as compared to case A (Fig. 5b). For kaolinite reaction (Fig. 7b), not only do the rates cover a smaller range than in case A (Fig. 6b), but the reaction occurs only in the precipitation direction. Such differences in pore-scale heterogeneities between the two cases are quantified by the differences in the range of concentration and reaction rates in Table 3.

6.3. Comparison between continuum-scale reaction rates

To illustrate the differences between the rates from the continuum model and the continuum-scale rates from the network model, Fig. 8 shows R_C and R_N as a function of time for the two reactive minerals in case A. The anorthite dissolution rate increases with time, due to the gradual influx of highly acidic aqueous phase from the boundary. Eventually, the system reaches steady state, where the aqueous concentrations and reaction rates become constants. The release of Ca^{2+},

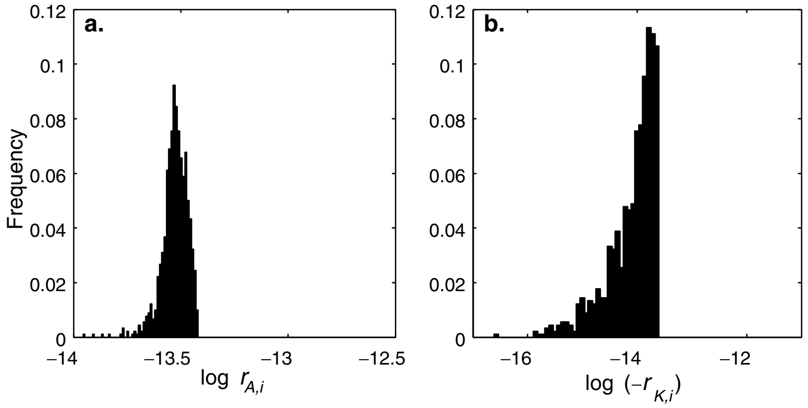

Fig. 7. Steady state reaction rate distributions in case B: anorthite dissolution rates (a) and kaolinite precipitation rates (b).

Table 3
Comparison of pore-scale heterogeneities between the two simulation scenarios

	$[Ca^{2+}]$	$[H^+]$	$r_{A,i}$	$r_{K,i}$
Case A	2.6	0.65	1.1	4.6
Case B	1.3	0.25	0.5	2.2

Values shown for each variable are the ranges in order of magnitude.

Al^{3+}, and H_4SiO_4 from anorthite dissolution leads to the oversaturation of the aqueous phase with respect to kaolinite. As such, kaolinite precipitates, and the increase in its precipitation rate parallels the increase in anorthite dissolution rate.

For each reactive mineral, the two models predict very different evolutions of the reaction rates. The continuum model overestimates the anorthite dissolution rate for the duration of the simulation. At steady state, it overestimates the rate by 30%. For kaolinite, the continuum model initially predicts its dissolution (although, these slightly positive values of R_C are difficult to see in Fig. 8b), which contradicts the prediction from the network model. Over time, the continuum model predicts kaolinite precipitation, but with a much smaller rate. At steady state, it underestimates the kaolinite precipitation rate by almost two orders of magnitude (with the ratio of R_C over R_N being 0.05). Overestimation of the anorthite dissolution rate and underestimation of kaolinite precipitation rate by the continuum model lead to an overestimation of the net dissolving rate of the solid phase by approximately a factor of 1.5 at steady state.

Fig. 9 shows a comparison of the time evolution of the rate calculated using volume-averaged concentration, R'_N, and the continuum-scale rate from the network model, R_N, for each mineral. The values of $R'_{N,A}$ underestimate those of $R_{N,A}$ at the very start of the simula-

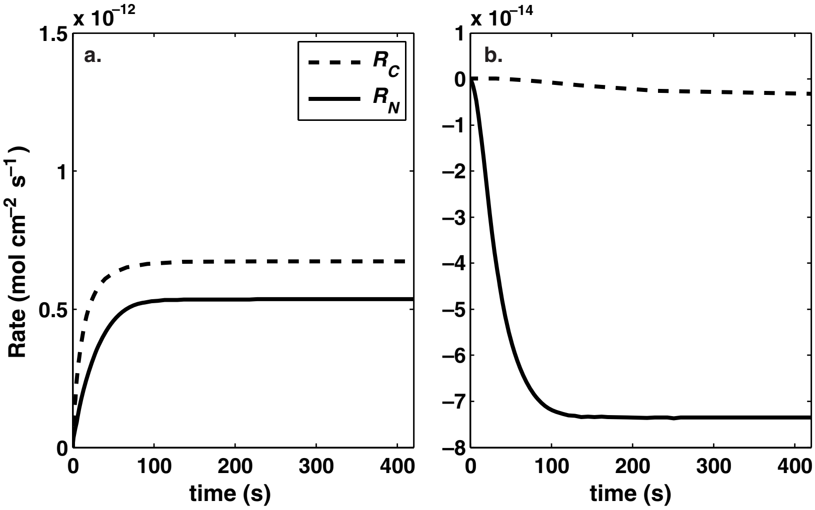

Fig. 8. For case A: comparison of R_C and R_N evolution for anorthite (a) and kaolinite (b).

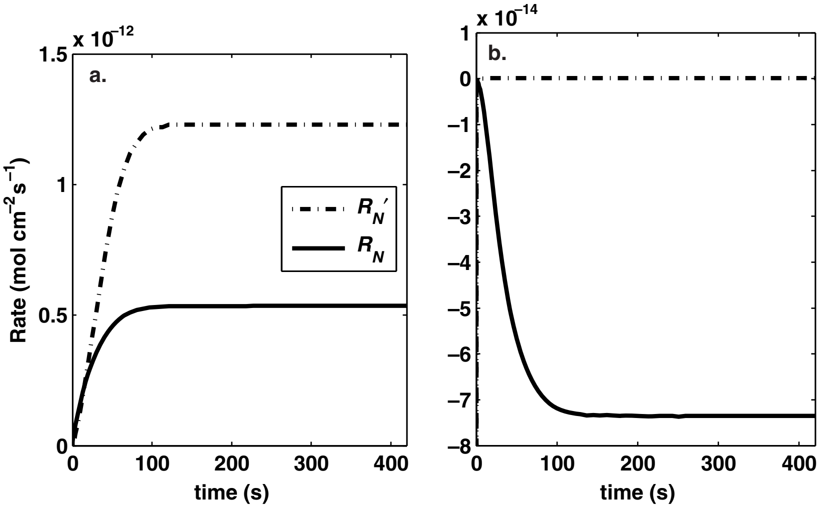

Fig. 9. For case A: comparison of R'_N and R_N evolution for anorthite (a) and kaolinite (b).

tion, and then significantly overestimate $R_{N,A}$. At steady state, the ratio of $R'_{N,A}$ over $R_{N,A}$ is 2.3. For kaolinite, $R'_{N,K}$ predicts its dissolution over the entire time period (although $R'_{N,K}$ is close to zero, it is actually positive), which is in contrast with the precipitation predicted by the network model. At steady state the ratio of $R'_{N,K}$ over $R_{N,K}$ is -1.8×10^{-3}. As such, values of $R'_{N,K}$ not only predict the wrong reaction rate, but also the wrong reaction direction.

Compared to those in case A, the differences between continuum-scale rates are much smaller in case B. Table 4 presents the differences between the continuum-scale rates for the two simulation scenarios, in terms of the ratios between continuum-scale reaction rates. For case B, these ratios are much closer to unity than in case A, which means that the scaling effect is much smaller. For example, the value of β_K is positive in case B, indicating the correct prediction of reaction direction by using volume-averaged concentrations. This smaller scaling effect is attributed to the less significant pore-scale variations in concentrations and reaction rates.

6.4. Equilibrium relationships at the continuum scale

As a result of pore-scale concentration heterogeneities, the equilibrium relationships for instantaneous reactions that are applicable at the pore scale may not hold at the continuum scale. For example, in aqueous solutions under the temperature, pressure, and salinity conditions of these simulations, the product of the activities of hydrogen ion and hydroxide ion equals the equilibrium constant 6.6×10^{-14}. However, the ionic activity product (IAP) values calculated from volume-averaged activities are not equal to their equilibrium constants. To illustrate this we show the temporal evolution of $\log \mathrm{IAP}$ in case A for the water dissociation reaction $H_2O \rightleftharpoons H^+ + OH^-$, and Al^{3+} speciation reaction $Al^{3+} + 4OH^- \rightleftharpoons Al(OH)_4^-$ in Fig. 10. For both reactions, the deviations of $\log \mathrm{IAP}$ from $\log K_{eq}$ are very large at an early time period, where the IAP values are orders of magnitude different from the values of the equilibrium constants. At steady state, the deviations reach constant values, IAP values 1.1 and 3.6 times their respective values of equilibrium constants for water and aluminum. In case B, the deviations of IAP values from equilibrium constants are much smaller. For example, at steady state, the IAP values are 1.0 and 1.2 times their respective values of equilibrium constants for water and aluminum.

Table 4
Comparison of the ratios of continuum-scale reaction rates for the two simulation scenarios

	η_A	η_K	β_A	β_K
Case A	1.3	0.046	2.3	−0.0018
Case B	1.1	0.56	1.2	0.089

7. Discussion

Simulation results have shown that under highly acidic conditions relevant to geological CO_2 sequestration, heterogeneities in physical and mineral properties can lead to pore-scale heterogeneities in concentrations and reaction rates, which results in scaling effects of reaction kinetics. With different boundary pH values, case A and case B differ significantly in the extent of the scaling effect. In both cases, the time scale of advection, calculated as the ratio of the network length to average flow velocity (L/q), is approximately 100 s. The diffusion time scale, calculated as the ratio of the square of the network

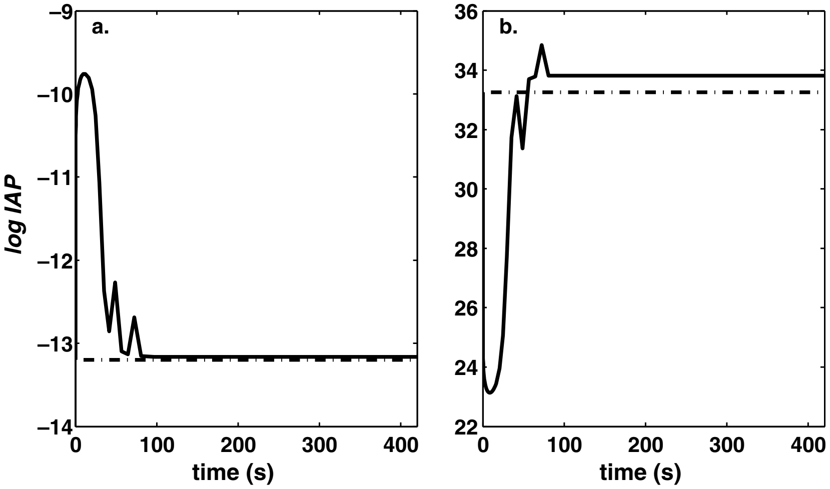

Fig. 10. Evolution of $\log \mathrm{IAP}$ for case A: (a) water dissociation reaction $H_2O = H^+ + OH^-$; (b) Al^{3+} speciation reaction $Al^{3+} + 4OH^- = Al(OH)_4^-$. The dashed lines indicate the value of $\log K_{eq}$ for each reaction.

length to the diffusion coefficient (L^2/D), is about 10^3–10^4 s. The time scale of reaction, however, differs in case A and B due to their different boundary pH values. For purpose of comparison, we estimate the time it would take for reaction alone to effect a change in concentration from the initial to the steady state condition. In case A, the steady-state anorthite dissolution rate is in the order of $10^{-10.6}$ mol s^{-1} (almost three orders of magnitude larger than the average rate in individual pores due to the much larger surface area of reactive minerals at the network scale). Initially the anorthite dissolution rate is orders of magnitude smaller because of the high initial pH values. Therefore, on average, the anorthite dissolution rate is about $10^{-10.9}$ mol s^{-1}. In case A, the concentrations of calcium varied from the initial 7.9×10^{-6} to 1.58×10^{-4} mol L^{-1} at steady state, which corresponds to a mass change of 8.9×10^{-10} mol. As such, the corresponding reaction time scale is 70 s, slightly smaller than the advection time scale. This means that the rates of advection and reaction are comparable, with none of them dominating. The comparable rates of reaction and advection lead to large spatial variations in concentrations, which results in relatively large scaling effect. In case B, due to the much larger pH value, the average anorthite dissolution rate is in the order of $10^{-12.7}$ mol s^{-1}, corresponding to a reaction time scale on the order of 10^3 s that is much larger than the advection time scale. Compared to case A, the extent of spatial variations in concentrations is much smaller, and the scaling effect is smaller.

With the same extent of spatial variations in concentrations, spatial variations in reaction rates can vary for different reactions, due to the difference in rate dependence on concentrations. In general, for a given range of spatial variation in concentration, the larger the rate dependence on concentration, the larger the spatial variation in local reaction rates. For the anorthite reaction, the very large range of calcium concentrations observed in case A has little effect on the spatial variation in rates, because in a system in which anorthite dissolution is highly thermodynamically favorable and under acidic conditions, the anorthite dissolution rate is dependent only on hydrogen ion concentration. Although the variation of hydrogen ion concentration in case A spans less than one order of magnitude, due to the nonlinear dependence of the anorthite dissolution rate on the hydrogen ion activities, the values of $r_{\mathrm{A},i}$ cover more than an order of magnitude. For case B, the nonlinear dependence of reaction rate on $\{\mathrm{H}^+\}$ also produces greater variability in the reaction rate, but the effect is much less important than in case A. For kaolinite precipitation, due to the high dependence of rates on hydrogen ion activity (raised to the power of −5.0), the pH variations lead to significant spatial variation in rates, spanning approximately five orders of magnitude in case A and two orders of magnitude in case B. Nonlinear dependence on activities of chemical species, especially on $\{\mathrm{H}^+\}$, is commonly observed for rate laws for mineral dissolution and precipitation reactions [9,87]. As such, we expect to see larger or smaller spatial variation in local reaction rates than those in local concentrations, depending on the mathematical form of the rate laws.

The very large spatial variation in local concentrations has significant implications for the error produced by reaction rates estimated using volume-averaged concentrations, as is analogous to what is done when interpreting field measurements using inverse modeling. The consumption of hydrogen ions from anorthite dissolution raises the pH such that the pH in reactive pores is higher than the pH in the non-reactive pores. However, volume averaging is a non-discriminating calculation that includes concentrations in both reactive and non-reactive pores. Because the reactive pores occupy only 10% of the network, the volume-averaged pH is more representative of pH in non-reactive pores, which underestimates the pH in reactive pores. Because chemical reaction rates depend only on concentrations in reactive pores, the concentrations in non-reactive pores play no role in driving or inhibiting the reaction rates in the porous medium (except indirectly via mass transport mechanisms). Therefore, although volume averaging produces concentrations that are true representations of the total mass of a species per total fluid volume, these values do not always serve as good indicators of the concentrations that drive the chemical reactions. Our work has shown that when volume-averaged concentrations are used in the prediction of continuum-scale reaction rates, significant errors can result and the scaling effect is large, especially in case A where there exist significant differences between concentrations in reactive and non-reactive pores. These errors led to the overestimation of the anorthite dissolution rate and the incorrect prediction of kaolinite reaction direction. In case B, with smaller discrepancies between concentrations in reactive and non-reactive pores, the scaling effect is much smaller.

A discrepancy between the reaction rate from the continuum model and that from the network model was also observed, especially in case A. This difference was less significant than the error produced from volume-averaging. The difference between R_C and R_N may appear to be small, however, this “small” difference in rates can lead to significant differences in predictions of the dynamics of reactive transport processes for a longer time scale. Overestimation of mineral dissolution rates by a factor of 2 will nominally lead to underestimation of reaction time scales by a factor of half. Furthermore, in models that predict long-term reaction progress, the overestimation of reaction rates will eventually overestimate the rates of porosity change. The strong dependence of permeability on porosity, often raised to the power of 3, can magnify the effects of the initial "small" difference in reaction rates to produce a considerable error in the predicted flow field. The overestimated flow rates will further produce even larger reaction rates. Therefore, the error in rates can amplify to a significant amount, and the continuum model may ultimately predict highly erroneous reactive transport dynamics relative to the true system.

The explanation for the discrepancy between R_C and R_N is slightly different than the explanation for the difference between R'_N and R_N. Pore-scale heterogeneities create concentration gradients that enhance the extent to which pore-to-pore mass transport of reactive species governs reaction kinetics. A continuum model, such as is used in forward modeling, is designed to ignore pore-scale heterogeneities, and mathematically represents the entire system as if it is well mixed. At a given point in time, the incoming fluid instantaneously comes in contact with all the reactive minerals in the system. Thus, the continuum model implicitly assumes no mass transport limitation at the pore scale. As such, it fails to capture the extent of spatial variations in concentration that arises from the slow mass transport of reactive species from pore to pore, especially in case A. In case B, with relatively small spatial variations in concentrations, the scaling effect is much smaller.

The results presented here are consistent with the observation of the lab-field discrepancy, that is, the direct use of reaction kinetics at scales larger than lab measurements often leads to the overestimation of reaction rates under natural conditions [12]. Although many factors, such as reaction duration, surface area and coating, have been considered as causes of such discrepancy [15], this work casts light on another potential factor: the spatial variations in physical and mineral properties of natural porous media. This work shows that spatial heterogeneities in physical and chemical properties do affect large-scale reaction rates under natural conditions, and the extrapolation of lab-measured reaction kinetics may need to incorporate the effect of such spatial heterogeneities.

The fact that the equilibrium relationships that apply at the pore scale may not hold at the continuum scale has potentially important implications for both forward and inverse modeling. In forward modeling, equilibrium relationships for instantaneous reactions are coupled with reaction rate laws for kinetic reactions to describe the reactive processes. In inverse modeling, equilibrium relationships are applied using measured aqueous concentrations in groundwater samples to infer the minerals that are dissolving, and the minerals that are precipitating. Both types of model can impose equilibrium relationships that do not really exist at the continuum scale.

Equilibrium relationships are theoretically established to describe chemical speciation in spatially uniform systems. If the pore-to-pore variations in concentrations are sufficiently large, as in case A, equilibrium relationships may not hold for the spatially-averaged concentrations used to describe continuum-scale phenomena in porous media. Such discrepancy has been encountered in many reaction and transport phenomena in subsurface systems (see [11], and references therein), and calls for efforts incorporating effects of porous medium heterogeneities in these relationships. This remains an open research question.

8. Summary and conclusions

This work establishes a novel methodology to use pore-scale network modeling to examine scaling effects in geochemical reaction rates. Pore-scale network models are constructed to represent the detailed physical and mineral properties of porous media. Reactive transport processes are simulated at the pore scale, and the continuum-scale reaction rate R_N is calculated for the entire network and is taken to be a measure of the "true" reaction rate. To explore the scaling effects, we also calculate two additional continuum-scale rates that ignore pore-scale heterogeneities and use the lab-measured reaction rates directly: R_C, the rate obtained through continuum modeling, and R'_N, the rate obtained using volume-averaged concentrations. Values of R_C are compared to R_N to examine the extent to which the continuum approach used in forward modeling would lead to erroneous prediction of reaction rates in porous media. Values of R'_N are compared with R_N to examine the extent to which field-measured concentrations, such as those used in inverse modeling, accurately predict the continuum-scale reaction rates.

The application of this method was illustrated with a pore-scale network model that represents a consolidated sandstone, with reactive minerals being anorthite and kaolinite occupying 10% of the pore space and gathering in pore clusters of size $2 \times 2 \times 15$. The network contains 9000 pores, corresponding to the spatial scale of several millimeters in *x*-, *y*-, *z*-direction. Simulations were run under conditions relevant to CO_2 sequestration: one with the boundary fluid in equilibrium with a high pressure of CO_2 (case A), and the other with a less amount of CO_2 (case B).

Simulation results have shown that in case A, the relatively large anorthite reaction rates arising from the highly acidic boundary fluid leads to order-of-magnitude spatial variations in concentrations and reaction rates, which can be poorly represented by uniform or averaged concentrations from models that ignore pore-scale heterogeneities. As such, the rates calculated from these single-valued concentrations in lab-measured reaction rate laws would introduce large errors and the scaling effects are significant. Under such conditions, the equilibrium relationships that apply at the pore scale may not hold at the continuum scale, which suggests that common practice of reactive transport simulations may impose equilibrium relationships that do not really exist at the continuum scale. In case B, with reduced acidity of boundary fluid, the magnitude of the pore-scale heterogeneities is much smaller than in case A, which eventually leads to smaller scaling effects. The differences in the scaling effects in the two cases suggest that elevated CO_2 concentrations can produce conditions under which scaling effects are significant.

These findings have potentially significant implications for reactive transport modeling. In general, the significance of pore-scale heterogeneity will depend on a variety of factors, including, for example, hydrodynamic conditions, and the total amount and spatial distributions of reactive minerals. Although the observed significance of the pore-scale heterogeneities and scaling effect are specific to our current network model and simulation conditions, the results imply that elevated CO_2 concentrations in deep aquifer systems can generate conditions under which scaling becomes important for reactive transport modeling. Under conditions where spatial heterogeneities exist and scaling becomes important, geochemical modeling must be approached carefully, and that general scaling laws incorporating the heterogeneity effect need to be developed.

Overall, pore-scale network modeling has proven to be an effective research tool to upscale reactive transport processes from the pore scale to the continuum scale. It allows for the investigation of details at the pore scale which cannot be done with traditional experimental studies, and thereby allows for identification of important pore-scale details that are essential to describe the reactive transport processes at the continuum scale. This novel application of pore-scale network modeling may be useful to study scaling issues associated with other geochemical reactions in heterogeneous porous media, and therefore is likely to provide new perspectives for resolving the long-standing lab-field rate discrepancy.

Disclaimer

This report was prepared as an account of work sponsored by an agency of the United States Government. Neither the United States Government nor any agency thereof, nor any of their employees, make any warranty, express or implied, or assumes any legal liability or responsibility for the accuracy, completeness, or usefulness of any information, apparatus, product, or process disclosed, or represents that its use would not infringe privately owned rights. Reference herein to any specific commercial product, process, or service by trade name, trademark, manufacturer, or otherwise does not necessarily constitute or imply its endorsement, recommendation, or favoring by the United States Government or any agency thereof. The views and opinions of authors expressed herein do not necessarily state or reflect those of the United States Government or any agency thereof.

Acknowledgements

This material is based upon work supported by the US, Department of Energy under Award No. DE-FG02-05ER15636. The authors also acknowledge BP and Ford Motor Co. for their support of the Carbon Mitigation Initiative at Princeton University.

Appendix A. Supplementary data

Supplementary data associated with this article can be found, in the online version at doi:10.1016/j.advwatres.2005.10.011.

References

[1] Steefel CI, Lasaga AC. A coupled model for transport of multiple chemical species and kinetic precipitation/dissolution reactions with application to reactive flow in single phase hydrothermal systems. Am J Sci 1994;294:529–92.

[2] Le Gallo Y, Bildstein O, Brosse E. Coupled reaction-flow modeling of diagenetic changes in reservoir permeability, porosity and mineral compositions. J Hydrol 1998;209(1–4):366–88.

[3] Bolton EW, Lasaga AC, Rye DM. Long-term flow/chemistry feedback in a porous medium with heterogeneous permeability: kinetic control of dissolution and precipitation. Am J Sci 1999; 299:1–68.

[4] Saunders JA, Toran LE. Modeling of radionuclide and heavy metal sorption around low- and high-pH waste disposal sites at Oak Ridge, TN. Appl Geochem 1995;10(6):673–84.

[5] Xu TF, White SP, Pruess K, Brimhall GH. Modeling of pyrite oxidation in saturated and unsaturated subsurface flow systems. Transp Porous Media 2000;39(1):25–56.

[6] Mayer AS, Kelley CT, Miller CT. Optimal design for problems involving flow and transport phenomena in saturated subsurface systems. Adv Water Resour 2002;25(8–12):1233–56.

[7] Metz V, Kienzler B, Schussler W. Geochemical evaluation of different groundwater–host rock systems for radioactive waste disposal. J Contam Hydrol 2003;61(1–4):265–79.

[8] Parkhurst DL, Plummer LN. Geochemical models. In: Alley WM, editor. Regional groundwater quality. New York: Van Nostrand Reinhold; 1993. p. 199–225.

[9] Lasaga AC. Kinetic theory in the earth sciences, Princeton series in geochemistry. Princeton: Princeton University Press; 1998.

[10] Tompson AFB, Jackson KJ. Reactive transport in heterogeneous systems: an overview. In: Lichtner PC, Steefel CI, Oelkers EH, editors. Reactive transport in porous media. Reviews in mineralogy, vol. 34. Washington, DC: Mineralogical Society of America; 1996. p. 269–310.

[11] Bryant SL, Thompson KE. Theory, modeling and experiment in reactive transport in porous media. Curr Opin Colloid Interface Sci 2001;6(3):217–22.

[12] White AF, Brantley SL. Chemical weathering rates of silicate minerals: an overview. In: White AF, Brantley SL, editors. Chemical weathering rates of silicate minerals. Reviews in mineralogy, vol. 31. Washington, DC: Mineralogical Society of America; 1995. p. 1–22.

[13] Murphy SF, Brantley SL, Blum AE, White AF, Dong HL. Chemical weathering in a tropical watershed, luquillo mountains, puerto rico: II. Rate and mechanism of biotite weathering. Geochim Cosmochim Acta 1998;62(2):227–43.

[14] Malmstrom ME, Destouni G, Banwart SA, Stromberg BHE. Resolving the scale-dependence of mineral weathering rates. Environ Sci Technol 2000;34(7):1375–8.

[15] White AF, Brantley SL. The effect of time on the weathering of silicate minerals: why do weathering rates differ in the laboratory and field? Chem Geol 2003;202(3–4):479–506.

[16] Malmstrom ME, Destouni G, Martinet P. Modeling expected solute concentration in randomly heterogeneous flow systems with multicomponent reactions. Environ Sci Technol 2004;38(9): 2673–9.

[17] Szecsody JE, Zachara JM, Chilakapati A, Jardine PM, Ferrency AS. Importance of flow and particle-scale heterogeneity on CoII/IIIEDTA reactive transport. J Hydrol 1998;209(1–4): 112–36.

[18] Lichtner PC, Tartakovsky DM. Stochastic analysis of effective rate constant for heterogeneous reactions. Stochastic Environ Res Risk Assess 2003;17(6):419–29.

[19] Fatt I. The network model of porous media i. Capillary characteristics. Pet Trans AIME 1956;207:144–59.

[20] Celia MA, Reeves PC, Ferrand LA. Recent advances in pore scale models for multiphase flow in porous-media. Rev Geophys 1995; 33:1049–57.

[21] Blunt MJ. Flow in porous media—pore-network models and multiphase flow. Curr Opin Colloid Interface Sci 2001;6(3): 197–207.

[22] Laurindo JB, Prat M. Numerical and experimental network study of evaporation in capillary porous media. Phase distributions. Chem Eng Sci 1996;51(23):5171–85.

[23] Laurindo JB, Prat M. Numerical and experimental network study of evaporation in capillary porous media. Drying rates. Chem Eng Sci 1998;53(12):2257–69.

[24] Tsimpanogiannis IN, Yortsos YC, Poulou S, Kanellopoulos N, Stubos AK. Scaling theory of drying in porous media. Phys Rev E 1999;59(4):4353–65.

[25] Prat M. Recent advances in pore-scale models for drying of porous media. Chem Eng J 2002;86(1–2):153–64.

[26] Carmeliet J, Descamps F, Houvenaghel G. A multiscale network model for simulating moisture transfer properties of porous media. Transp Porous Media 1999;35(1):67–88.

[27] Stark J, Manga M. The motion of long bubbles in a network of tubes. Transp Porous Media 2000;40(2):201–18.

[28] Jia C, Shing K, Yortsos YC. Visualization and simulation of non-aqueous phase liquids solubilization in pore networks. J Contam Hydrol 1999;35(4):363–87.

[29] Dillard LA, Blunt MJ. Development of a pore network simulation model to study nonaqueous phase liquid dissolution. Water Resour Res 2000;36(2):439–54.

[30] Zhou DG, Dillard LA, Blunt MJ. A physically based model of dissolution of nonaqueous phase liquids in the saturated zone. Transp Porous Media 2000;39(2):227–55.

[31] Held RJ, Celia MA. Pore-scale modeling and upscaling of nonaqueous phase liquid mass transfer. Water Resour Res 2001; 37(3):539–49.

[32] Knutson CE, Werth CJ, Valocchi AJ. Pore-scale modeling of dissolution from variably distributed nonaqueous phase liquid blobs. Water Resour Res 2001;37(12):2951–63.

[33] Suchomel BJ, Chen BM, Allen MB. Network model of flow, transport and biofilm effects in porous media. Transp Porous Media 1998;30(1):1–23.

[34] Suchomel BJ, Chen BM, Allen MB. Macroscale properties of porous media from a network model of biofilm processes. Transp Porous Media 1998;31(1):39–66.

[35] Kim D-S, Fogler H. Biomass evolution in porous media and its effects on permeability under starvation conditions. Biotechnol Bioeng 2000;69(1):47–56.

[36] Dupin HJ, Kitanidis PK, McCarty PL. Pore-scale modeling of biological clogging due to aggregate expansion: a material mechanics approach. Water Resour Res 2001;37(12):2965–79.

[37] Dupin HJ, Kitanidis PK, McCarty PL. Simulations of two-dimensional modeling of biomass aggregate growth in network models. Water Resour Res 2001;37(12):2981–94.

[38] Stewart T, Fogler H. Biomass plug development and propagation in porous media. Biotechnol Bioeng 2001;72(3):353–63.

[39] Sugita F, Gillham RW, Mase C. Pore scale variation in retardation factor as a cause of nonideal reactive breakthrough curves. 2. Pore network analysis. Water Resour Res 1995;31(1): 113–9.

[40] Acharya RC, Van der Zee S, Leijnse A. Transport modeling of nonlinearly adsorbing solutes in physically heterogeneous pore networks. Water Resour Res 2005;41(2):W02020. doi:10.1029/2004WR003500.

[41] Fredd C, Fogler H. Influence of transport and reaction on wormhole formation in porous media. AIChE J 1998;44(9): 1933–49.

[42] Bachu S, Gunter WD, Perkins EH. Aquifer disposal of CO_2: hydrodynamic and mineral trapping. Energy Convers Manage 1994;35(4):269–79.

[43] Giammar DE, Bruant RG, Peters CA. Forsterite dissolution and magnesite precipitation at conditions relevant for deep saline aquifer storage and sequestration of carbon dioxide. Chem Geol 2005;217(3–4):257–76.

[44] Bruant J, Robert G, Celia MA, Guswa AJ, Peters CA. Safe storage of CO_2 in deep saline aquifers. Environ Sci Technol 2002; 36(11):240A–5A.

[45] Walker J, Hays PB, Kasting JF. A negative feedback mechanism for the long term stabilization of earth's surface temperatures. J Geophys Res-Solid Earth 1981;86:9776–82.

[46] Berner RA, Lasaga AC, Garrels RM. The carbonate–silicate geochemical cycle and its effect on atmospheric carbon dioxide over the past 100 million years. Am J Sci 1983;283:641–83.

[47] Brady PV. The effect of silicate weathering on global temperature and atmospheric CO_2. J Geophys Res-Solid Earth 1991;96(B11): 18101–6.

[48] Gunter WD, Perkins EH, Hutcheon I. Aquifer disposal of acid gases: modelling of water–rock reactions for trapping of acid wastes. Appl Geochem 2000;15(8):1085–95.

[49] Xu T, Apps JA, Pruess K. Reactive geochemical transport simulation to study mineral trapping for CO_2 disposal in deep arenaceous formations. J Geophys Res-Solid Earth 2003;108(B2): 2071.

[50] Johnson JW, Nitao JJ, Knauss KG. Reactive transport modeling of CO_2 storage in saline aquifers to elucidate fundamental processes, trapping mechanisms, and sequestration partitioning. In: Baines SJ, Worden RH, editors. Geological storage of carbon dioxide. Special Publications, vol. 233. London: Geological Society of London; 2004. p. 107–28.

[51] Rochelle CA, Czernichowski-Lauriol I, Milodowski AE. The impact of chemical reactions on CO_2 storage in geological formations: a brief review. In: Baines SJ, Worden RH, editors. Geological storage of carbon dioxide. Special Publication, vol. 233. London: Geological Society of London; 2004. p. 87–106.

[52] Wieland E, Stumm W. Dissolution kinetics of kaolinite in acidic aqueous-solutions at 25-degrees-C. Geochim Cosmochim Acta 1992;56(9):3339–55.

[53] Oelkers EH, Schott J, Devidal J-L. The effect of aluminum, pH, and chemical affinity on the rates of aluminosilicate dissolution reactions. Geochim Cosmochim Acta 1994;58(9):2011–24.

[54] Blum AE, Stillings LL. Feldspar dissolution kinetics. In: White AF, Brantley SL, editors. Chemical weathering rates of silicate

minerals. Reviews in mineralogy, vol. 31. Washington, DC: Mineralogical Soc America; 1992. p. 291–351.

[55] Amrhein C, Suarez DL. The use of a surface complexation model to describe the kinetics of ligand-promoted dissolution of anorthite. Geochim Cosmochim Acta 1988;52(12):2785–93.

[56] Brady PV, Walther JV. Controls on silicate dissolution rates in neutral and basic pH solutions at 25-degrees-C. Geochim Cosmochim Acta 1989;53(11):2823–30.

[57] Oelkers EH, Schott J. Experimental study of anorthite dissolution and the relative mechanism of feldspar hydrolysis. Geochim Cosmochim Acta 1995;59(24):5039–53.

[58] Helgeson HC, Murphy WM, Aagaard P. Thermodynamic and kinetic constraints on reaction-rates among minerals and aqueous-solutions. 2. Rate constants, effective surface-area, and the hydrolysis of feldspar. Geochim Cosmochim Acta 1984;48(12): 2405–32.

[59] Ganor J, Mogollon JL, Lasaga AC. The effect of pH on kaolinite dissolution rates and on activation-energy. Geochim Cosmochim Acta 1995;59(6):1037–52.

[60] Carroll SA, Walther JV. Kaolinite dissolution at 25-Degrees-C, 60-Degrees-C, and 80-Degrees-C. Am J Sci 1990;290(7):797–810.

[61] Nagy KL, Blum AE, Lasaga AC. Dissolution and precipitation kinetics of kaolinite at 80-Degrees-C and pH 3—the dependence on solution saturation state. Am J Sci 1991;291(7):649–86.

[62] Knapp RB. Spatial and temporal scales of local equilibrium in dynamic fluid–rock systems. Geochim Cosmochim Acta 1989;53: 1955–64.

[63] Lichtner PC. Continuum model for simultaneous chemical-reactions and mass-transport in hydrothermal systems. Geochim Cosmochim Acta 1985;49(3):779–800.

[64] Lichtner PC. Continuum formulation of multicomponent–multiphase reactive transport. In: Lichtner PC, Steefel CI, Oelkers EH, editors. Reactive transport in porous media. Reviews in mineralogy, vol. 34. Washington, DC: Mineralogical society of America; 1996. p. 1–81.

[65] Cussler EL. Diffusion: mass transfer in fluid systems. 2nd ed. Cambridge, United Kingdom: Cambridge University Press; 1997.

[66] Stumm W, Morgan JJ. Aquatic chemistry: chemical equilibria and rates in natural waters. 3rd ed. New York: Environmental Science & Technology, Wiley; 1996.

[67] Freeze RA, Cherry JA. Groundwater. Upper Saddle River: - Prentice Hall, Inc.; 1979.

[68] Turcke MA, Kueper BH. Geostatistical analysis of the borden aquifer hydraulic conductivity field. J Hydrol 1996;178(1–4): 223–40.

[69] Lindquist WB, Venkatarangan A, Dunsmuir J, Wong TF. Pore and throat size distributions measured from synchrotron X-ray tomographic images of fontainebleau sandstones. J Geophys Res-Solid Earth 2000;105(B9):21509–27.

[70] Freeze RA. A stochastic-conceptual analysis of one-dimensional groundwater flow in nonuniform homogeneous media. Water Resour Res 1975;11:725–41.

[71] Lymberopoulos DP, Payatakes AC. Derivation of topological, geometrical, and correlational properties of porous-media from pore-chart analysis of serial section data. J Colloid Interface Sci 1992;150(1):61–80.

[72] Wardlaw NC, Li Y, Forbes D. Pore-throat size correlation from capillary-pressure curves. Transp Porous Media 1987;2(6): 597–614.

[73] Ross SM. Introduction to probability models. 7th ed. San Diego, CA: Academic Press; 2000.

[74] Sen PN, Straley C, Kenyon W, Wittingham MS. Surface-to-volume ratio, charge density, nuclear magnetic relaxation, and permeability in clay-bearing sandstones. Geophysics 1990;55(1): 61–9.

[75] Borgia GC, Brown RJS, Fantazzini P. Nuclear magnetic resonance relaxivity and surface-to-volume ratio in porous media with a wide distribution of pore sizes. J Appl Phys 1996;79(7): 3656–64.

[76] Frosch GP, Tillich JE, Haselmeier R, Holz M, Althaus E. Probing the pore space of geothermal reservoir sandstones by nuclear magnetic resonance. Geothermics 2000;29(6):671–87.

[77] Blatt H. Sedimentary petrology. 2nd ed. New York: W.H. Freeman and company; 1992.

[78] Steefel CI, MacQuarrie KTB. Approaches to modeling of reactive transport in porous media. In: Lichtner PC, Steefel CI, Oelkers EH, editors. Reactive transport in porous media. Reviews in mineralogy, vol. 34. Washington, DC: The Mineralogical Society of America; 1996. p. 83–130.

[79] Van der Hoven SJ, Solomon DK, Moline GR. Natural spatial and temporal variations in groundwater chemistry in fractured, sedimentary rocks: scale and implications for solute transport. Appl Geochem 2005;20:861–73.

[80] Duan Z, Sun R. An improved model calculating CO_2 solubility in pure water and aqueous NaCl solutions from 273 to 533 K and from 0 to 2000 bar. Chem Geol 2003;193(3–4):257–71.

[81] Morel F, Hering JG. Principles and applications of aquatic chemistry. New York: Wiley; 1993.

[82] Johnson JW, Oelkers EH, Helgeson HC. SUPCRT92: a software package for calculating the standard molal thermodynamic properties of minerals, gases, aqueous species, and reactions from 1 to 5000 bar and 0 to 1000 degC. Comput Geosci 1992;18(7): 899–947.

[83] Bourbie T, Zinszner B. Hydraulic and acoustic properties as a function of porosity in fontainebleau sandstone. J Geophys Res 1985;90:11,524–32.

[84] Zhu W, David C, Wong T. Network modeling of permeability evolution during cementation and hot isostatic pressing. Geophys Res: Solid Earth 1995;100(B8):15,451–64.

[85] Zhu WL, Evans B, Bernabe Y. Densification and permeability reduction in hot-pressed calcite: a kinetic model. J Geophys Res-Solid Earth 1999;104(B11):25501–11.

[86] Press WH, Teukolsky SA, Vetterling WT, Flannery BP. Numerical recipes in FORTRAN. 2nd ed. Cambridge: Cambridge University Press; 1992.

[87] Kump LR, Brantley SL, Arthur MA. Chemical weathering, atmospheric CO_2, and climate. Annu Rev Earth Planet Sci 2000; 28:611–67.